Article

Thin Reinforced Anion-Exchange Membranes for Non-Aqueous Redox Flow Battery Employing Fe/Co-Metal Complex Redox Species

Hyeon-Bee Song [1], Do-Hyeong Kim [1], Myung-Jin Lee [2] and Moon-Sung Kang [1,*]

[1] Department of Green Chemical Engineering, College of Engineering, Sangmyung University, Cheonan 31066, Republic of Korea; 2020d3008@sangmyung.kr (H.-B.S.); dohyeongkim665@gmail.com (D.-H.K.)
[2] Battery Material Technical Unit, Samsung Advanced Institute of Technology, Suwon 16678, Republic of Korea; alberto.lee@samsung.com
[*] Correspondence: solar@smu.ac.kr; Tel.: +82-41-550-5383

Abstract: Non-aqueous redox flow batteries (NARFBs) have been attracting much attention because they can significantly increase power and energy density compared to conventional RFBs. In this study, novel pore-filled anion-exchange membranes (PFAEMs) for application to a NAPFB employing metal polypyridyl complexes (i.e., $Fe(bpy)_3^{2+}/Fe(bpy)_3^{3+}$ and $Co(bpy)_3^{2+}/Co(bpy)_3^{3+}$) as the redox species are successfully developed. A porous polyethylene support with excellent solvent resistance and mechanical strength is used for membrane fabrication. The PFAEMs are prepared by filling an ionic liquid monomer containing an imidazolium group and a crosslinking agent into the pores of the support film and then performing in situ photopolymerization. As a result, the prepared membranes exhibit excellent mechanical strength and stability in a non-aqueous medium as well as high ion conductivity. In addition, a low crossover rate for redox ion species is observed for the prepared membranes because they have relatively low swelling characteristics in non-aqueous electrolyte solutions and low affinity for the metal-complex redox species compared to a commercial membrane. Consequently, the PFAEM is revealed to possess superior battery performance than a commercial membrane in the NARFB tests, showing high energy efficiency of about 85% and stable operation for 100 cycles.

Keywords: non-aqueous redox flow batteries; pore-filled anion-exchange membranes; ionic liquid monomer; porous polyethylene support; in situ photopolymerization; metal polypyridyl complexes

1. Introduction

The growing concern over environmental pollution worldwide and the increasing demand for energy have heightened the focus on eco-friendly renewable energy sources. However, most renewable energy sources, such as solar and wind power, generate intermittent and inconsistent power, posing challenges in providing a stable energy supply. Hence, the development of inexpensive and reliable energy storage systems is crucial. Such systems can effectively utilize renewable energy sources and facilitate their integration into the power grid [1]. In this context, redox flow batteries (RFBs) have emerged as promising energy storage systems. RFBs, which use redox-active species dissolved in a solvent, are capable of storing large amounts of electricity [1–3]. Furthermore, they are increasingly recognized for their advantages, including scalability, long life cycle, reliability, and cost-effectiveness, making them a significant focus in the field of energy storage [4].

Generally, RFBs can be categorized into aqueous systems, employing water as the electrolyte solvent, and non-aqueous systems, utilizing organic solvents. In the case of aqueous RFBs, redox systems such as iron-chromium (Fe-Cr), zinc-bromide (Zn-Br), and all-vanadium (V) have been widely employed [5]. Notably, the all-vanadium and Zn-Br RFBs

are the most extensively developed representative technologies. Aqueous RFBs employing commonly used electrolytes currently exhibit a relatively low energy density ranging from 20 to 50 Wh/L. The energy density of RFBs is proportional to the cell voltage and the solubility of redox couples. In the case of conventional aqueous RFBs, the operating voltage is limited due to concerns about the occurrence of water decomposition (at 1.23 V in theory). Hence, non-aqueous RFBs (NARFBs) employing organic solvents, capable of providing a broader electrochemical window, are advantageous in achieving high energy density [6]. In other words, NARFBs have the merit of broadening the range of selection of redox materials suitable for high-voltage operation compared to aqueous RFBs [7–11]. Furthermore, the organic solvents employed in NARFBs can provide either low freezing or elevated boiling points, thereby extending the operating temperature range of the RFBs [12].

Meanwhile, metal coordination complexes (MCC) are actively being studied as redox-active materials for NARFBs. MCC, in comparison to ionic metal salts, are favored in polar organic solvents due to their heightened solubility, attributed to chelation with organic ligands. Noteworthy ligands include acetylacetone (acac) alongside nitrogen-containing ligands such as phenanthroline (phen), terpyridine (terpy), and bipyridine (bpy), each participating effectively in chelation for enhanced solubility. In particular, nitrogen-containing ligands exhibit remarkable affinity and stability in forming coordinated complexes with various transition metals, prominently including V, Fe, Co, Ni, and Cu [13].

The organic solvents commonly employed in the fabrication of non-aqueous electrolytes for NARFBs encompass acetonitrile (ACN) and propylene carbonate (PC), with *N*-methyl-2-pyrrolidone (NMP), dichloromethane (DCM), and tetrahydrofuran (THF) also being viable alternatives. Among these, PC has the widest temperature range between freezing and boiling points and the electrochemical window, which can create more favorable conditions for operating high-energy density NARFBs [14]. Meanwhile, given the typically low ion conductivity in organic solvents, including a supporting electrolyte becomes imperative to enhance ion conductivity in these solvents. As supporting anions, tetrafluoroborate (BF_4^-), perchlorate (ClO_4^-), and hexafluorophosphate (PF_6^-) are mainly used because they have relatively small ionic radii (0.229, 0.237, and 0.254 nm, respectively) and high ionic conductivity [15]. Among them, however, ClO_4^- can be excluded from consideration due to its explosive hazards. As for supporting cations, tetraalkylammonium species are commonly employed, and akin to the supporting anions, a smaller ionic radius correlates with higher limiting ion conductivity. Notably, tetramethylammonium (Me_4N^+), tetraethylammonium (Et_4N^+), and tetrapropylammonium (Pr_4N^+) cations exhibit reduced ionic radii (0.283, 0.343, and 0.381 nm, respectively), resulting in elevated limiting molar conductivity [15].

Meanwhile, a membrane, one of the key components of NARFB, separates the anolyte and catholyte while allowing the transport of counter ions to maintain overall charge neutrality during operation [10,11]. Furthermore, the application of an ideal membrane significantly influences the RFB performances, yielding Coulombic efficiencies approaching 100% and high current densities. The representative type of membrane used in NARFB is ion-exchange membranes (IEMs). IEMs are generally made of organic polymers with ion exchangeable fixed charge groups, selectively permitting the transport of counter ions while electrostatically excluding co-ions [16]. For designing high-performance RFBs, a pivotal consideration involves maintaining charge balance in electrochemical cells during operation while minimizing the crossover of active species between the anolyte and catholyte. This crossover can cause self-discharge, reducing energy efficiency and causing permanent loss of battery capacity [17]. Notably, the prevalent use of cations as redox-active species in electrolytes poses challenges in mitigating their undesired transport through the membrane, particularly when employing cation-exchange membranes (CEMs). In this case, an anion-exchange membrane (AEM) may be preferable for use in RFB as a barrier [13,18]. Additionally, one of the problems in applying IEMs to NARFB is that general membranes are designed to be used in aqueous environments, so they have low ionic conductivity and poor stability in non-aqueous environments. In conclusion, an IEM

suitable for NARFB should have high ion conductivity in non-aqueous solutions, a low crossover rate of redox-active species, and excellent durability [19]. Therefore, the IEMs for NARFB are being developed from this perspective. For instance, Li et al. have fabricated an AEM by brominating poly(2,6-dimethyl-1,4-phenylene oxide) (PPO) and subsequently introducing ion exchange groups into the brominated PPO (BPPO). The anion exchange groups were incorporated using 4,4′-bipyridine as a crosslinking agent, allowing simultaneous control over ion exchange capacity (IEC) and crosslinking degree, depending on the content. The fabricated membrane was applied in a NARFB incorporating the active species of tetrakis(acetonitrile)copper(I) bis(trifluoromethylsulfonyl)imide ([Cu(MeCN)$_4$][Tf$_2$N]), demonstrating comparable performance to the commercial membrane (Morgane-ADP) [11]. Kwon et al. developed AEMs based on poly(arylene ether ketone) (PAEK) crosslinked with alkyl chains containing quaternary ammonium groups. The IEC and nanostructure of the synthesized anion-exchange polymer were controlled by varying the content of the crosslinking agent. The results showed that the prepared AEM exhibited excellent BF$_4^-$ ion conductivity, and the solvent swelling stability and mechanical and chemical durability of the membrane could be improved by introducing the crosslinking structure [20]. Additionally, Mazumder et al. fabricated a UV-cured AEM based on phenyl acrylate and conducted a comparative analysis with the commercial Fuma-375 membrane to assess long-term performance. The results revealed that after the 1000th charge/discharge cycles, the RFB using a commercially available membrane, Fuma-375, retained about 28% of its initial capacity, while that using a fabricated membrane showed a total capacity retention of 55% due to a relatively low crossover rate [21].

From the literature survey, it was determined that although electrolytes and IEMs for some non-aqueous systems have been studied, not enough research results have been reported for commercialization, and in particular, there is a lack of research related to the optimal design of IEMs for NARFB applications. Therefore, in this study, we aimed to derive the design factors of IEMs suitable for NARFBs. Figure 1 exhibits the operation principle for the NARFB studied in this work. Fe(bpy)$_3^{2+/3+}$ and Co(bpy)$_3^{2+/3+}$ redox couples were chosen as the cathode and anode active materials, respectively, among promising metal-organic ligand complex redox couples. These redox couples exhibited a redox potential of about 2.16 V and stable redox properties for 100 cycles [22,23]. PC was employed as the solvent for the electrolyte, while tetraethylammonium tetrafluoroborate (TEABF$_4$) served as the supporting electrolyte. Meanwhile, IEMs can be fabricated using various methods, among which pore-filled IEMs (PFIEMs) are gaining significant attention. The PFIEMs are fabricated by filling the pores of porous support with an ionomer, offering numerous advantages over traditional IEMs. The PFIEMs exhibit excellent physical strength despite their thin membrane thickness and have advantages such as low area resistance, high chemical stability, and low membrane fabrication cost, so they are being investigated for application in various energy conversion technologies as well as desalination processes [16,24]. Therefore, we fabricated and utilized a pore-filled AEM (PFAEM) with a thickness of approximately 25 μm, characterized by low resistance in non-aqueous media, to realize high-performance NARFBs. 1-Allyl-3-butylimidazolium tetrafluoroborate (ABIMBF$_4$) and *N,N*-dimethylacrylamide (DMAA) were selected as monomers for the preparation of the anion-exchange polymer, and a dimethacrylate-based crosslinking agent was used to enhance the mechanical and chemical stability of the membrane. The monomer composition allowed for the preparation of a mixture without additional solvents and enabled the one-pot fabrication of the anion-exchange polymer without the need for post-treatment processing. The prepared membranes were systematically analyzed using various membrane characterizations, and their performance was also confirmed using NARFB cell experiments.
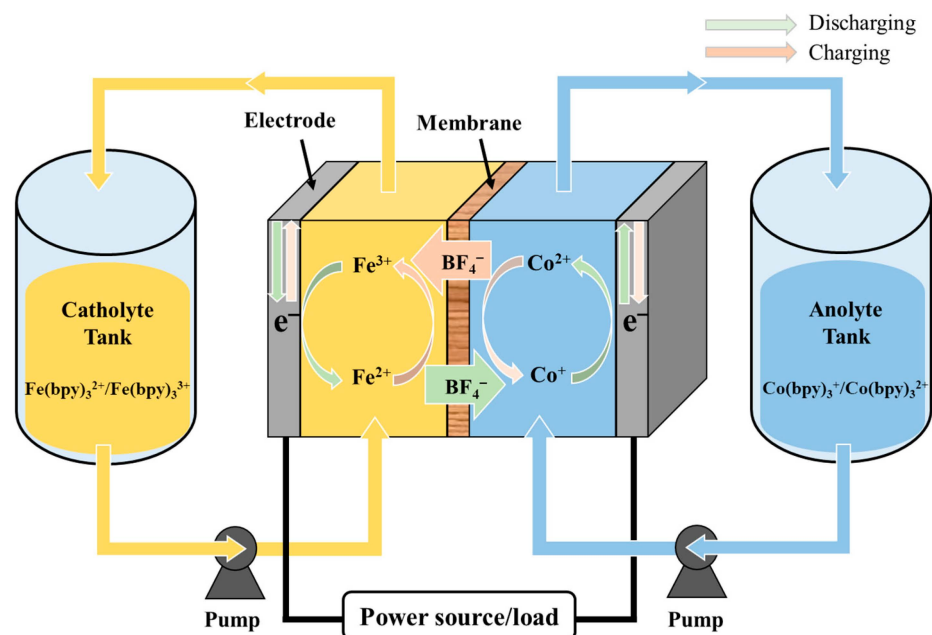
Figure 1. Schematic drawing of operation principle for NARFB employing $Fe(bpy)_3^{2+/3+}$ and $Co(bpy)_3^{2+/3+}$ redox couples.

2. Materials and Methods

2.1. Materials

As mentioned, $ABIMBF_4$ (Kanto Chemical Co., INC., Tokyo, Japan) and DMAA (Sigma–Aldrich, St. Louis, MO, USA) were employed as the monomers to prepare the PFAEMs. The crosslinking agents tested were ethylene glycol dimethacrylate (EGDMA), 1,3-butanediol dimethacrylate (BDDMA), 1,6-hexanediol dimethacrylate (HDDMA), and bisphenol A dimethacrylate (BPADMA). The chemical structures and molecular weights of the crosslinking agents used are summarized in Table 1. Additionally, benzophenone (BP) was employed as a photoinitiator. All the crosslinking reagents and photoinitiators were purchased from Sigma-Aldrich (St. Louis, MO, USA) and used without further purification.

Table 1. Chemical structures and molecular weights of hydrophilic crosslinking agents used.

Name	Chemical Structure	Mw (g/mol)
Ethylene glycol dimethacrylate (EGDMA)		198.22
1,3-Butanediol dimethacrylate (BDDMA)		226.27
1,6-Hexanediol dimethacrylate (HDDMA)		254.32
Bisphenol A dimethacrylate (BPADMA)		364.43

A polyethylene (PE) porous film (Hipore, t = 25 μm, Asahi Kasei E-materials Corp., Tokyo, Japan) was used as a support for the fabrication of the reinforced membrane. In addition, FAP4 (Fumatech, Baden-Württemberg, Germany) was chosen as a commercial membrane for comparing the membrane characteristics and NARFB performance of the fabricated PFAEMs.

2.2. Membrane Fabrication

The PFAEMs were fabricated using various molar ratios of ABIMBF$_4$ and DMAA for subsequent characterization. ABIMBF$_4$ was mixed with DMAA at the molar ratios (ABIMBF$_4$/DMAA) of 0.1, 0.2, 0.4, 0.6, 0.8, and 1, respectively. Following this, regardless of the monomer ratios, the content of the crosslinking agent was varied in the range of 3–6 wt% of the total monomers, and the photoinitiator (BP) was incorporated at a concentration of 2 wt%. The PE porous film was then immersed in the prepared ionomer solution. The PE porous film was then immersed in the prepared ionomer solution. After sufficient impregnation to fill the pores, the membrane was placed between release films and photopolymerized for 15 min in a chamber equipped with a 1 kW UV lamp (UV-CB-1.5X1, Wonil Science, Daejeon, Republic of Korea). The membrane was then separated from release films and stored in an aqueous NaCl solution or non-aqueous electrolyte solution, depending on the test's purposes. The preparation process and molecular structure of the anion-exchange polymer synthesized in this study are illustrated in Figure 2.
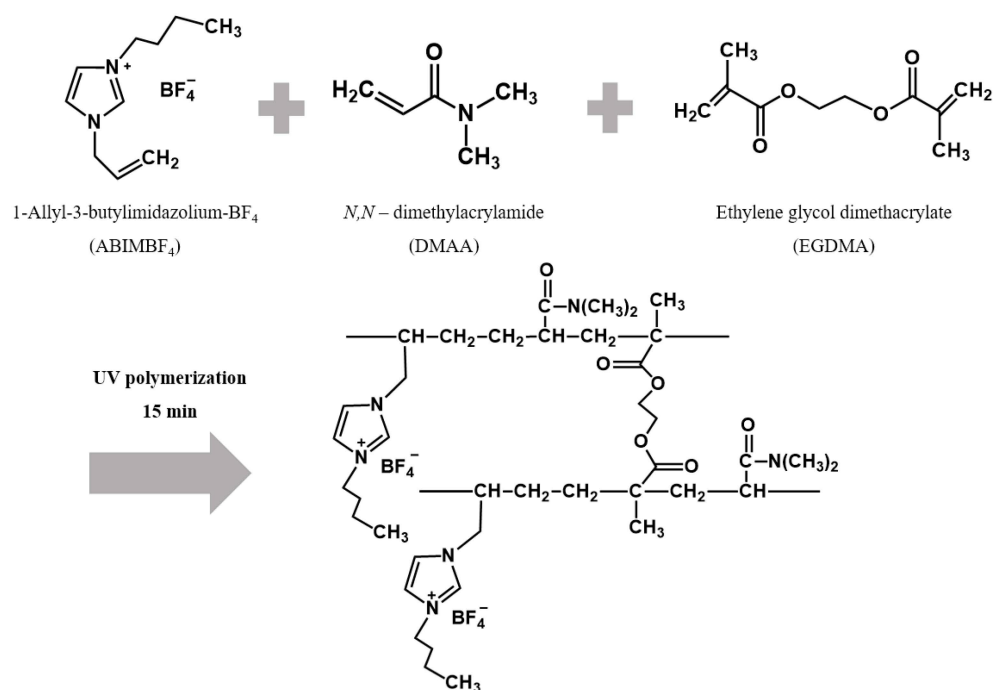

Figure 2. Reaction scheme for preparing crosslinked anion-exchange polymer.

2.3. Membrane Chacterizations

Fourier transform infrared spectroscopy (FT/IR-4700, JASCO, Tokyo, Japan) was used to confirm the molecular structure of the prepared membranes and the introduction of ion exchange groups. Herein, the average data obtained from 16 scans at a resolution of 4 cm^{-1} were analyzed.

Field emission scanning electron microscopy (FE-SEM, MIRA LMH, TESCAN, Brno, Czech Republic) analysis was conducted to observe the morphological characteristics of the prepared membrane. The surface and cross-section of the porous PE support and the PFAEM were measured at magnifications of 20.00 kx and 30.00 kx, respectively.

To evaluate the mechanical properties of the membranes, the commercial and prepared membranes were cut into pieces of 5 × 2.5 cm^2 in the wet state. The tensile strength and

elongation were measured using a universal testing system (Instron 3343, Instron, Norwood, MA, USA).

The thermal stability of the porous support and the prepared PFAEMs was measured using a thermogravimetric analyzer (TGA-50, Shimadzu Co., Kyoto, Japan) with nitrogen purging in the range of 30–600 °C at a temperature increase rate of 10 °C/min.

The membrane electrical resistance (MER) was measured using a lab-made clip cell and a potentiostat/galvanostat (SP-150, Bio-logic science Instruments, Seyssinet-Pariset, France) with an impedance measurement module. The blank resistance (R_2) was measured by immersing the clip cell in a 0.5 M NaCl aqueous solution, and the resistance (R_1), which includes the membrane resistance, was measured after inserting the membrane sample in the clip cell. The measured resistance values were substituted into Equation (1) to calculate the MER value [25]:

$$\text{MER} = (R_1 - R_2) \times A \left[\Omega \cdot \text{cm}^2 \right] \tag{1}$$

where A is the effective membrane area (cm^2).

Meanwhile, the ionic conductivity (σ) is inversely proportional to the area resistance of the membrane and was calculated by Equation (2) [26]:

$$\sigma = \frac{L}{\text{MER}} \left[\frac{\text{S}}{\text{cm}} \right] \tag{2}$$

where L is the membrane thickness (cm).

To measure water uptake (WU), samples were cut into 2×2 cm^2 pieces and immersed in distilled water until equilibrium was reached. The surface moisture of the membrane was removed, and the weight of the wet sample (W_{wet}) was measured. The sample was then dried in an 80 °C dry oven for over 12 h, and the weight of the dry sample (W_{dry}) was recorded. The WU was calculated by substituting the measured weight values into Equation (3) [26]:

$$WU = \frac{W_{wet} - W_{dry}}{W_{dry}} \times 100 \, [\%]. \tag{3}$$

In addition, solution uptake (SR) was evaluated using samples immersed in 1 M TEABF$_4$/PC, following the same method.

To measure the IEC, the membrane of Cl$^-$–form was converted to SO$_4$$^{2-}$–form by immersing in Na$_2SO_4$ solution for more than 6 h. The chloride ion concentration of the solution was determined by titration with silver nitrate, and finally, the dry weight of the membrane was measured, and the IEC was calculated by substituting the measured values into Equation (4) [26]:

$$\text{IEC} = \frac{C \cdot V_s}{W_{dry}} \left[\frac{\text{meq.}}{\text{g}_{\text{dry memb}}} \right] \tag{4}$$

where W_{dry} is the weight of the dried membrane, V_s is the volume of AgNO$_3$ standard solution used for titration, and C is the normal concentration of AgNO$_3$ standard solution.

The transport number (TN) was determined using the electromotive force (emf) method, which measures the diffusion potential across the membrane. The membrane potential (E_m) between solutions of differing concentrations was measured, and the TN was calculated based on the difference between the experimental and theoretical values. A membrane was positioned in the center of a 2-compartment cell, using 0.001 M and 0.005 M NaCl solutions as electrolytes. The membrane potential was measured using a digital voltmeter connected to a pair of Ag/AgCl electrodes. The measured potential values were then substituted into Equation (5) to determine the TN [27]:

$$E_m = \frac{RT}{F} (1 - 2t_a) \ln \frac{C_1}{C_2} \tag{5}$$

where t_a is the transport number for anion, R is the gas constant, T is the absolute temperature, F is the Faraday constant, and C_1 and C_2 are the concentrations of the NaCl solution, which were 1 mM and 5 mM, respectively.

Current-voltage (I–V) curves were measured by filling each side of a two-compartment cell with 140 mL of 0.025 M NaCl, placing a pair of Ag/AgCl reference electrodes on either side of the membrane, and applying voltage from 0 to 5 V at a rate of 10 mV/s using a potentiostat/galvanostat (SP-150, Bio-logic science Instruments, Seyssinet-Pariset, France). The obtained I–V curve was then analyzed to determine the limit current density (LCD) value [28].

Additionally, chronopotentiometry was conducted with the same experimental setup, applying a constant current density of 4.456 mA/cm^2 and measuring the voltage over 100 s. From the obtained chronopotentiometric curve, the transition time (τ) at which concentration polarization occurs was determined. The fraction of the conductive region (ε) on the membrane surface was then determined using Equation (6) [27]:

$$\varepsilon = \frac{2i\tau^{1/2}\left(t^m - t^b\right)}{C^b\, z\, F(\pi D)^{1/2}} \tag{6}$$

where i is the current density, z is the valence of counter ion, F is the Faraday constant, D is the diffusion coefficient, t^m and t^b are the TNs in membrane and solution, respectively, and C^b is the concentration of NaCl solution (0.025 M).

2.4. NARFB Performance Tests

The redox ion crossover rate of the membrane was measured using a two-compartment flowing cell made of Teflon material. The effective area of the membrane was 16 cm^2, and the membrane to be measured was inserted into the center of the cell and clamped. The permeation experiment was performed by circulating 230 mL each of PC solution (permeate) and 0.5 M Fe(bpy)$_3$(BF$_4$)$_2$/PC solution (feed). Samples were periodically collected from the permeate compartment, and the concentration of Fe(bpy)$_3{}^{2+}$ ions was determined using UV/vis spectroscopy (UV-2600, SHIMADZU, Tokyo, Japan) at the absorption wavelength of 522 nm. Finally, the permeability (P), used to determine the crossover rate of active species through the membrane, was calculated based on the time-dependent concentration changes of ions using Equation (7) [29]:

$$P = \frac{V_B L}{A(C_A - C_B(t))}\frac{dC_B(t)}{dt} \tag{7}$$

where C_A is the concentration of metal ion species in the feed compartment, $C_B(t)$ is the concentration of metal ion species in the permeate compartment at time t, V_B is the solution volume in the permeate compartment, and L and A are the thickness (cm) and effective area (cm^2) of the membrane, respectively.

A lab-made cell was used to evaluate the charge–discharge performance of commercial and manufactured membranes in non-aqueous systems. Figure 3 shows a schematic representation of the structure of the NARFB cell used in this study. For the operation of the NARFB, a 0.2 M Co(bpy)$_3$(BF$_4$)$_2$/0.5 M TEABF$_4$/PC solution was used as the anolyte, and a 0.2 M Fe(bpy)$_3$(BF$_4$)$_2$/0.5 M TEABF$_4$/PC solution was employed as the catholyte. Co(bpy)$_3$(BF$_4$)$_2$ and Fe(bpy)$_3$(BF$_4$)$_2$ were purchased from Hanchem (Daejeon, Republic of Korea), TEABF$_4$ from Sigma-Aldrich (St. Louis, MO, USA), and PC from Panax Etec (Nonsan, Republic of Korea) and used as received. An automatic battery cycler (WBCS 3000, Wonatech, Seoul, Republic of Korea) was used for charging/discharging in the voltage range of 1.7–2.3 V. The effective area of the electrode and membrane was 12.5 cm^2, and the current was controlled in the range of 10–20 mA. Carbon felt (GF20-3, Nippon Graphite, Otsu, Japan) was used as the electrode. To enhance the wettability of the electrode, it was thermally treated with a hot air blower at 400 °C for 20 min and then at 500 °C for 10 min

before being thoroughly soaked in the electrolyte. Meanwhile, the cyclability test was conducted by circulating 200 mL of catholyte (0.2 M Fe(bpy)$_3$(BF$_4$)$_2$/0.5 M TEABF$_4$/PC) and anolyte (0.2 M Co(bpy)$_3$(BF$_4$)$_2$/0.5 M TEABF$_4$/PC) solutions into the NARFB cell at a flow rate of 65 mL/min. A total of 100 cycles were run and evaluated at a current density of 1.2 mA/cm^2. For the charge/discharge performance evaluation, the Coulombic efficiency (CE), voltage efficiency (VE), and energy efficiency (EE) were calculated through Equations (8)–(10), respectively [30].

$$CE = \frac{\text{Discharge capacity (Ah)}}{\text{Charge capacity (Ah)}} \times 100 \ [\%] \tag{8}$$

$$VE = \frac{\text{Average discharge voltage (V)}}{\text{Average charge voltage (V)}} \times 100 \ [\%] \tag{9}$$
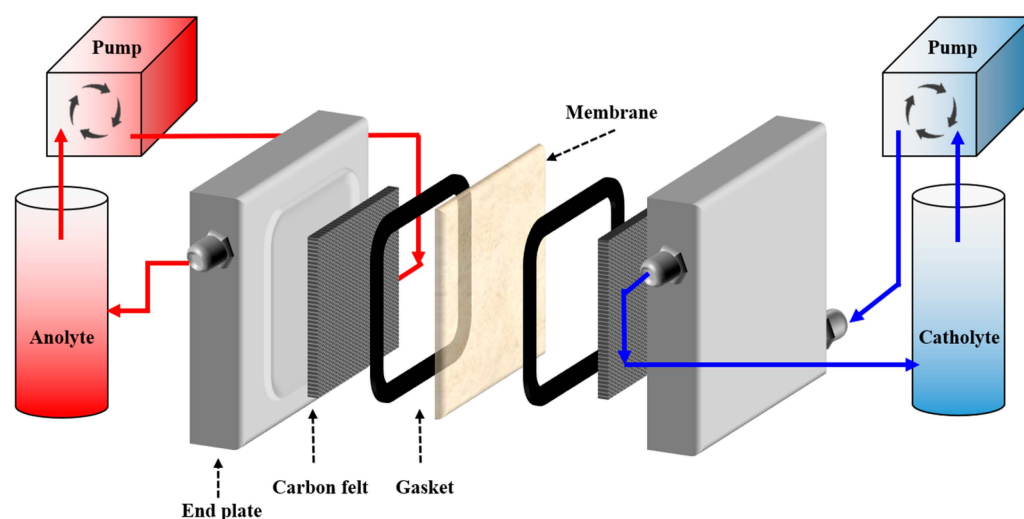
$$EE = CE \times VE \ [\%] \tag{10}$$

Figure 3. Schematic drawing of NARFB cell employed in this study (red line: anolyte stream; blue line: catholyte stream).

3. Results and Discussion

Figure 4 presents the surface and cross-sectional images of the PE porous support before ionomer filling and the fabricated PFAEM. The surface and cross-sectional FE-SEM images of PFAEM reveal that the pores in the porous support have been densely filled with polymers, resulting in a membrane structure that is uniformly dense without defects. This implies that during the membrane fabrication process, the monomers filled in the pores of the support underwent in situ reactions, leading to their polymerization.

The FT-IR spectra for the structural confirmation of the PE porous support and the prepared pore-filled membranes are shown in Figure 5. As revealed from the FT-IR spectra, characteristic absorption bands, not visible in the PE porous support, can be observed in the fabricated PFAEMs. The C-H absorption band identified at 2968 cm^{-1} represents the stretching vibration of the imidazole ring [31]. The presence of imidazolium groups in the fabricated membrane can also be confirmed by the stretching vibration of the C=N bond at 1566 cm^{-1} and the bending vibration of the imidazole rings at 761 cm^{-1} [32]. In addition, the peaks corresponding to the C=O bond at 1640 cm^{-1} and the C-O-C bond at 1120 cm^{-1} can be identified and attributed to the DMAA and crosslinker structures [33,34]. Unlike other crosslinking agents, BPADMA contains benzene rings, so the =C-H aryl stretching vibration of aromatics was additionally confirmed at 3030 cm^{-1} [35]. Furthermore, the increase in C=C absorption peak intensity around 1740 cm^{-1} is thought to be due to the benzene rings included in the BPADMA crosslinker [36]. Thus, the FT-IR spectral

analysis confirms that the porous PE support has been combined with the crosslinked anion-exchange polymer, including imidazolium groups, thereby indicating the successful fabrication of the PFAEMs.
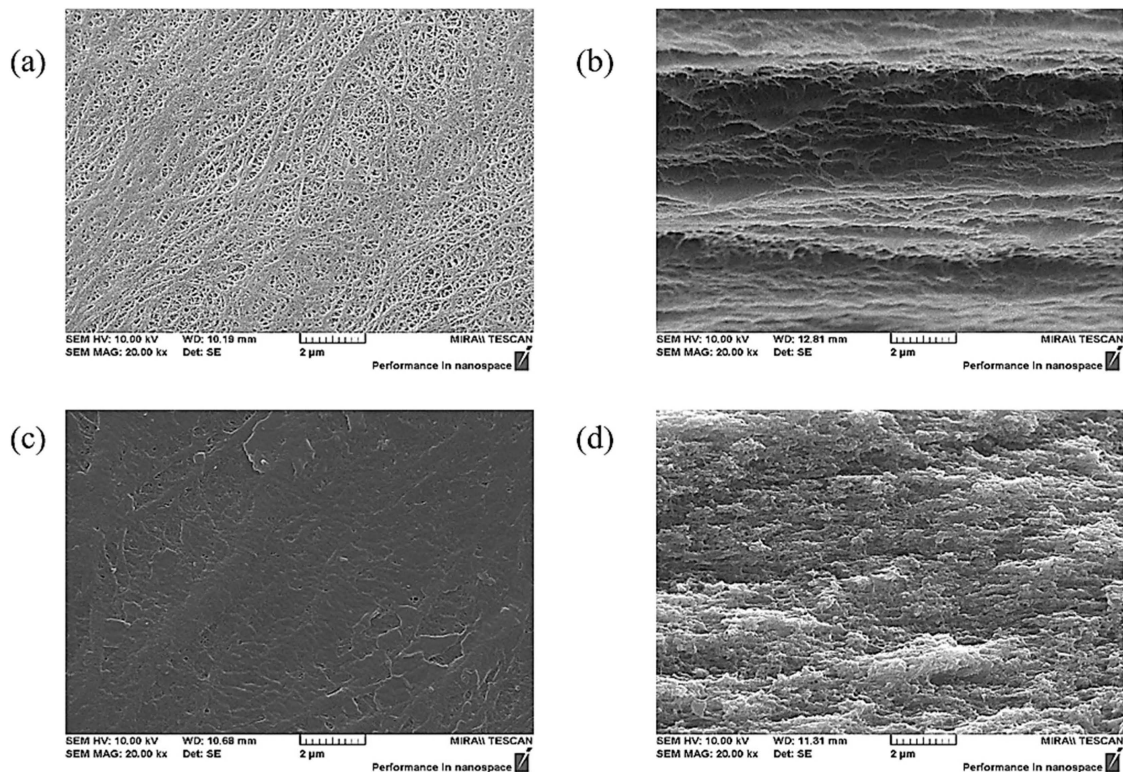

Figure 4. FE-SEM images: (**a**) surface and (**b**) cross-section of PE porous film; (**c**) surface and (**d**) cross-section of PFAEM.
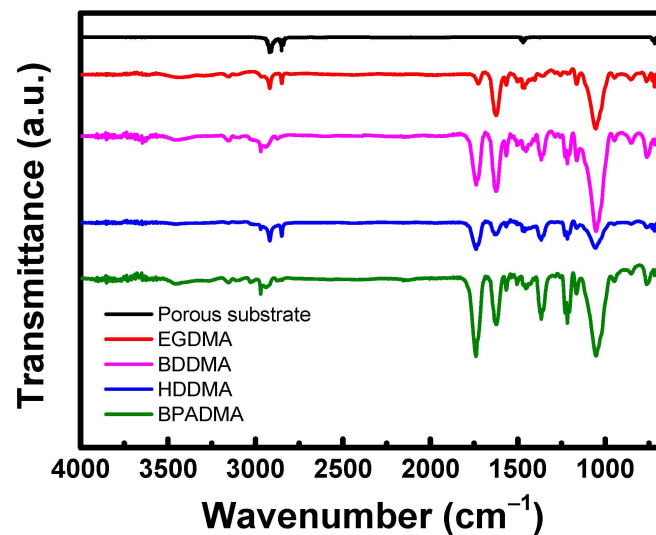

Figure 5. FT-IR spectra of PE porous support and PFAEMs prepared with different crosslinkers.

Meanwhile, the crosslinking of the ion-exchange polymer is crucial for enhancing its durability. Particularly for use in electrolyte environments involving organic solvents, chemical crosslinking of the membranes is essential. Therefore, in this study, four types of crosslinking agents with similar chemical structures but differing molecular weights were examined. The characteristics of the commercial membrane and PFAEMs prepared with different crosslinking agents are summarized in Table 2. From the experimental

results, no clear tendency could be confirmed depending on the molecular structure and molecular weight of the crosslinking agents. This is believed to be because the structure and molecular weight of the crosslinking agents have a complex effect on the characteristics of the membranes. However, it was again confirmed that regardless of the type of crosslinkers used, the difference in resistance in aqueous and non-aqueous electrolytes was significantly smaller compared to the commercial membrane. While the commercial membrane exhibited an approximately tenfold increase in resistance, all the fabricated membranes showed less than a twofold increase. Among the tested membranes, the PFAEM crosslinked with EGDMA (PFAEM–EGDMA) exhibited the lowest MER and TN values. Consequently, all membranes in subsequent experiments were fabricated using EGDMA as the crosslinker.

Table 2. Characteristics of commercial membrane and PFAEMs prepared with different crosslinkers (3 wt%).

Membranes	Thickness (μm)	IEC (meq./g)	WU (%)	MER [1] (Ω cm^2)	MER [2] (Ω cm^2)	TN (-)
FAP4 (Fumatech)	50	0.71	16.0	2.86	28.6	0.946
PFAEM–EGDMA	25	1.92	61.1	1.44	1.87	0.956
PFAEM–BDDMA	25	1.95	59.3	1.60	3.02	0.944
PFAEM–HDDMA	25	1.78	64.6	1.50	2.84	0.946
PFAEM–BPADMA	25	1.59	56.9	1.45	2.76	0.928

[1] MER measured in 0.5 M NaCl aqueous solution. [2] MER measured in 0.5 M TEABF$_4$/PC solution.

The tensile strength and elongation of the commercial membrane, the PE porous support, and the fabricated membrane (ABIMBF$_4$:DMAA = 1:1; crosslinked with 3 wt% EGDMA) were compared and summarized in Table 3. Primarily, due to the superior mechanical strength of the porous support used in membrane fabrication, the tensile strength and elongation of the fabricated PFAEM were found to be exceptionally high. Furthermore, the PFAEM filled with crosslinked ionomer exhibited an increase in tensile strength due to the elevated density compared to the PE porous support, although there was a slight decrease in elongation [37]. As a result, the prepared PFAEMs exhibited more than three times higher tensile strength and five times higher elongation compared to the commercial membrane.

Table 3. Mechanical properties of commercial membrane, PE porous support, and PFAEM crosslinked with EGDMA.

Membranes	Tensile Strength (MPa)	Elongation at Break (%)
FAP4 (Fumatech)	46.2	14.5
Porous support	154.0	88.3
PFAEM	166.1	76.2

Thermogravimetric analysis (TGA) was performed to evaluate the thermal stability of the prepared membrane (ABIMBF$_4$:DMAA = 1:1; crosslinked with 3 wt% EGDMA). As shown in Figure 6, the decomposition of the polymer backbone of the PE support began at around 450 °C. It can be seen that the prepared PFAEM was thermally stable up to about 250 °C, although a slight weight loss was observed due to the removal of water adsorbed on the membrane. Furthermore, a significant weight loss was observed above 250 °C due to the degradation of quaternary ammonium groups, and the weight loss above 450 °C was determined to be due to the degradation of the PE support and ionomer backbone [38].
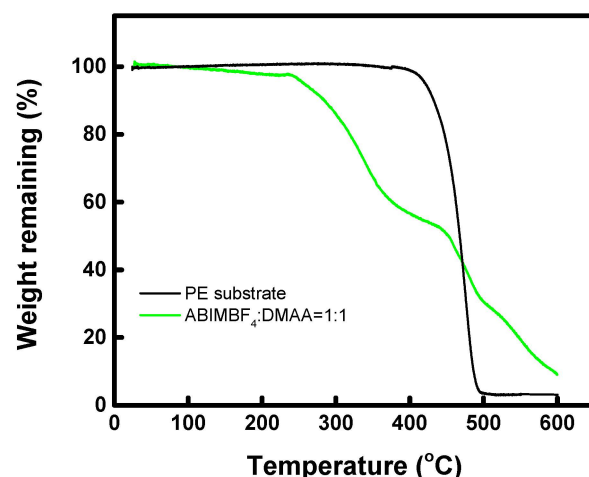
Figure 6. TGA curves of porous PE substrate and prepared PFAEM.

The electrical resistances of the commercial membrane and prepared PFAEM (ABIMBF$_4$: DMAA = 1:1; crosslinked with 3 wt% EGDMA) were measured in various electrolyte solutions, and the results are shown in Figure 7. It could be predicted that the prepared membrane (t = 25 μm) would exhibit lower electrical resistance due to the thinner film thickness compared to the commercial membrane (t = 50 μm). In actuality, in 0.5 M NaCl aqueous solution, the membranes displayed electrical resistance proportional to their thickness. However, in 0.5 M TEABF$_4$ aqueous solution, the PFAEM showed no significant difference in electrical resistance compared to the NaCl aqueous condition, while the commercial membrane, FAP4, exhibited a considerable increase in electrical resistance. Similarly, in 0.5 M TEABF$_4$/PC solution, the PFAEM did not demonstrate a substantial increase in resistance, in contrast to FAP4, which showed a significant increase. The differences in electrical resistance of the FAP4 membrane with different electrolytes can be attributed to the size difference between Cl$^-$ (235 pm as radius) and BF$_4^-$ (270 pm as radius) ions [39]. Consequently, the ionic radius of BF$_4^-$ is larger than that of Cl$^-$, leading to a greater mass transfer resistance of BF$_4^-$ ions through the membrane compared to Cl$^-$ ions [40,41]. However, the resistance of the fabricated membrane did not significantly increase regardless of the type of electrolyte solution used. This difference can be explained from the perspective of molecular imprinting effects, as the anion-exchange polymer in the fabricated membrane was synthesized using monomers containing BF$_4^-$ counter ions [42]. In addition, the electrical resistance of the PFAEMs measured in non-aqueous TEABF$_4$ solutions was found to be sufficiently low, similar to the results obtained in aqueous electrolyte solutions. Since the transport of BF$_4^-$ ions dominate the charge–discharge performance of the NARFB system in this study, the lower transport resistance of BF$_4^-$ ions through the membrane in the non-aqueous electrolyte may contribute to lowering the resistance of the system and improving the charge–discharge performance.

To reduce the undesired permeation of metal ion species through the membranes, the content of EGDMA was increased to 6 wt%. The PFAEMs were prepared by varying the molar ratio of ABIMBF$_4$ and DMAA, and the main characteristics of the fabricated membranes are summarized in Table 4. To maintain the high BF$_4^-$ ion transport characteristic due to the previously described molecular imprinting effect while achieving superior barrier performance, the membranes were fabricated with a reduced ratio of ABIMBF$_4$ compared to DMAA. The results exhibited that as the proportion of ABIMBF$_4$ increased, there was a tendency for an increase in the IEC, WU, and SU values while the MER decreased. This can be interpreted as an increase in affinity towards polar solvents due to the increased content of imidazolium groups, leading to an increase in free volume and a decrease in ion transport resistance [43]. Meanwhile, a significant change in resistance and ion conductivity in non-aqueous electrolytes was observed at molar ratios of ABIMBF$_4$/DMAA below 0.2. This suggests that as the content of ABIMBF$_4$ decreases, the free volume of the ionomer

drops below a certain threshold, resulting in substantial resistance to the transport of BF_4^- ions through the membrane.
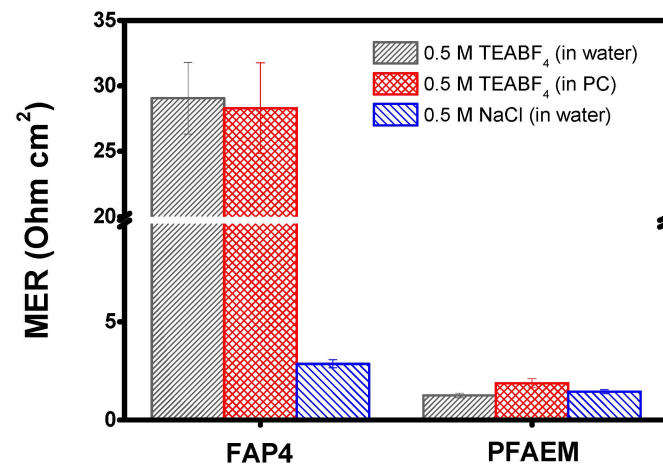

Figure 7. Resistance changes of commercial membrane and PFAEM ($ABIMBF_4$:DMAA = 1:1) with types of electrolyte solution.

Table 4. Characteristics of PFAEMs prepared with various molar ratios of $ABIMBF_4$:DMAA (crosslinked with 6 wt% EGDMA).

$ABIMBF_4$:DMAA (Mole Ratio)	IEC (meq./g)	WU (%)	SU (%)	MER [1] (Ω cm^2)	σ [2] (mS/cm)
0.1:1	1.25	29.6	25.0	76.7	0.033
0.2:1	1.38	27.8	24.7	43.5	0.057
0.4:1	1.55	29.7	35.6	9.41	0.276
0.6:1	1.78	50.2	44.1	3.31	0.756
0.8:1	1.79	55.7	48.4	2.99	0.870
1.0:1	1.90	56.2	53.9	2.15	1.011

[1] MER measured in 0.5 M $TEABF_4$/PC solution. [2] Ion conductivity measured in 0.5 M $TEABF_4$/PC solution (membrane thickness = 25 μm).

The performance evaluation of NARFBs employing PFAEMs fabricated at various $ABIMBF_4$ to DMAA molar ratios was carried out up to 10 cycles (C-1 to C-10), and the obtained charge–discharge curves are depicted in Figure 8. Since all the experimental conditions were the same except for the membrane, it can be deduced that the charge–discharge performance of NARFB is mainly determined by the characteristics of the membranes used. The results showed that typical charge–discharge curves were obtained up to the $ABIMBF_4$:DMAA ratio of 0.4:1. However, abnormal charge–discharge characteristics were observed at the $ABIMBF_4$/DMAA molar ratios lower than 0.2.

For a more detailed evaluation of NARFB performance, the charge–discharge efficiency was calculated for each cycle, and the results are shown in Figure 9. In the case of CE, which reflects the crossover of redox-active substances through the membrane [17], the PFAEMs with high $ABIMBF_4$ ratios above 0.8 exhibited relatively low values, and the highest values were obtained when the molar ratio of $ABIMBF_4$/DMAA was in the range of 0.4–0.6. The VE value, reflecting the impact of the MER, tended to increase with higher $ABIMBF_4$:DMAA molar ratios. However, it did not show a significant difference above the $ABIMBF_4$/DMAA = 0.4 molar ratio and maintained a high value of over 90%. This indicates that while compositions with higher $ABIMBF_4$/DMAA ratios benefit from lower MER, thereby offering some advantages in terms of VE, they also exhibit a higher rate of redox species crossover, leading to a greater reduction in CE. As a result, the optimal charge/discharge performance was achieved when the molar ratio of $ABIMBF_4$ to DMAA was in the range of 0.4–0.6:1. As mentioned earlier, below the $ABIMBF_4$/DMAA = 0.2 molar

ratio, normal charge–discharge efficiency cannot be achieved due to the excessive MER. The NARFB cell employing PFAEM exhibited a maximum energy efficiency of about 80%, which was superior to that of the commercial membrane FAP4 (Figure 9d). This improved performance is attributed to the thin membrane thickness and high affinity for BF_4^- ions, resulting in lower MER. Additionally, appropriate crosslinking contributed to reducing the crossover rate of redox ion species.
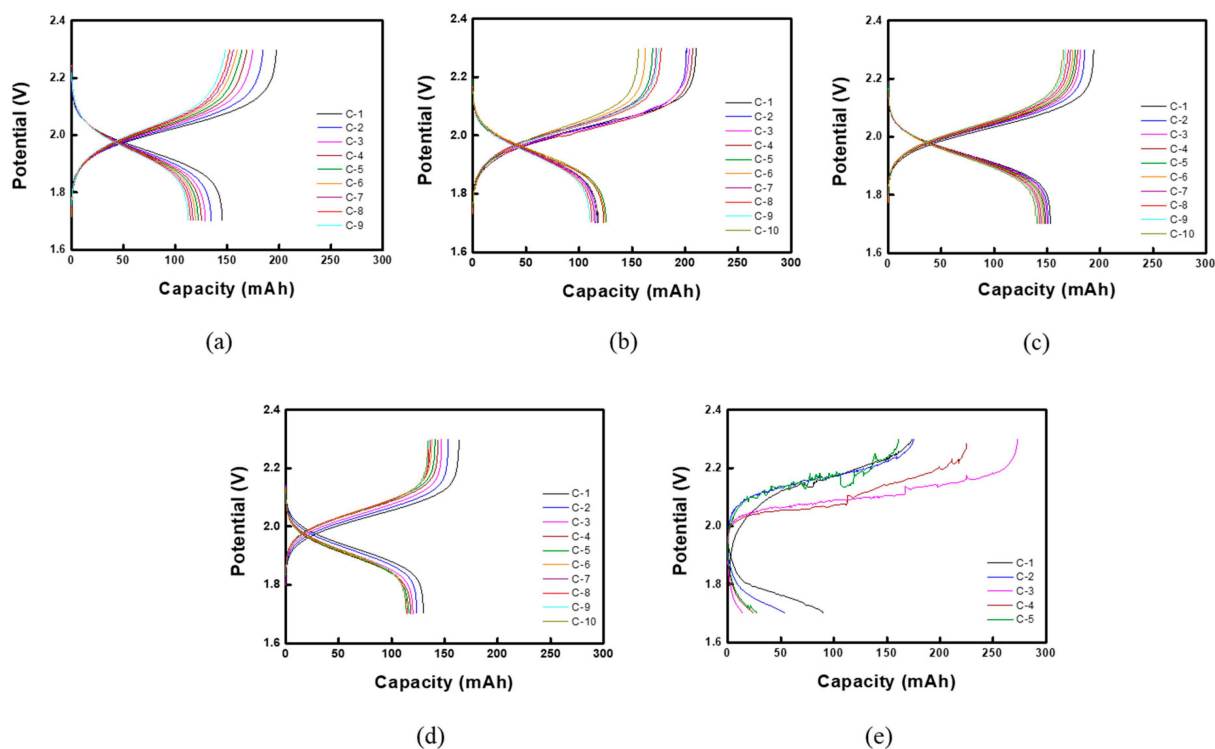

(a)

(b)

(c)

(d)

(e)

Figure 8. Charging-discharging curves of NARFBs employing PFAEMs prepared with different molar ratios of $ABIMBF_4$:DMAA: (**a**) 1:1, (**b**) 0.8:1, (**c**) 0.6:1, (**d**) 0.4:1, and (**e**) 0.2:1.

As such, the crossover of redox ion species through the membrane causes energy efficiency and capacity losses, which is an important property to consider in membrane fabrication [13,17]. The results of the permeability measurements of the redox ion species ($Fe(bpy)_3^{2+}$) for the commercial membrane and the PFAEM ($ABIMBF_4$:DMAA = 0.6:1), which exhibited the most superior charge–discharge performance in NARFB, are summarized in Table 5. The results revealed that the permeability of redox ions through the PFAEM was significantly lower compared to the commercial membrane. This finding is consistent with the CE results measured in the NARFB experiments. Additionally, this implies that the fabricated PFAEM, compared to the commercial membrane, has a lower affinity for metal complex ions in non-aqueous media and possesses an appropriate degree of crosslinking to suppress undesirable redox species crossover [44].

Table 5. Permeability of redox ion species through membranes in organic medium.

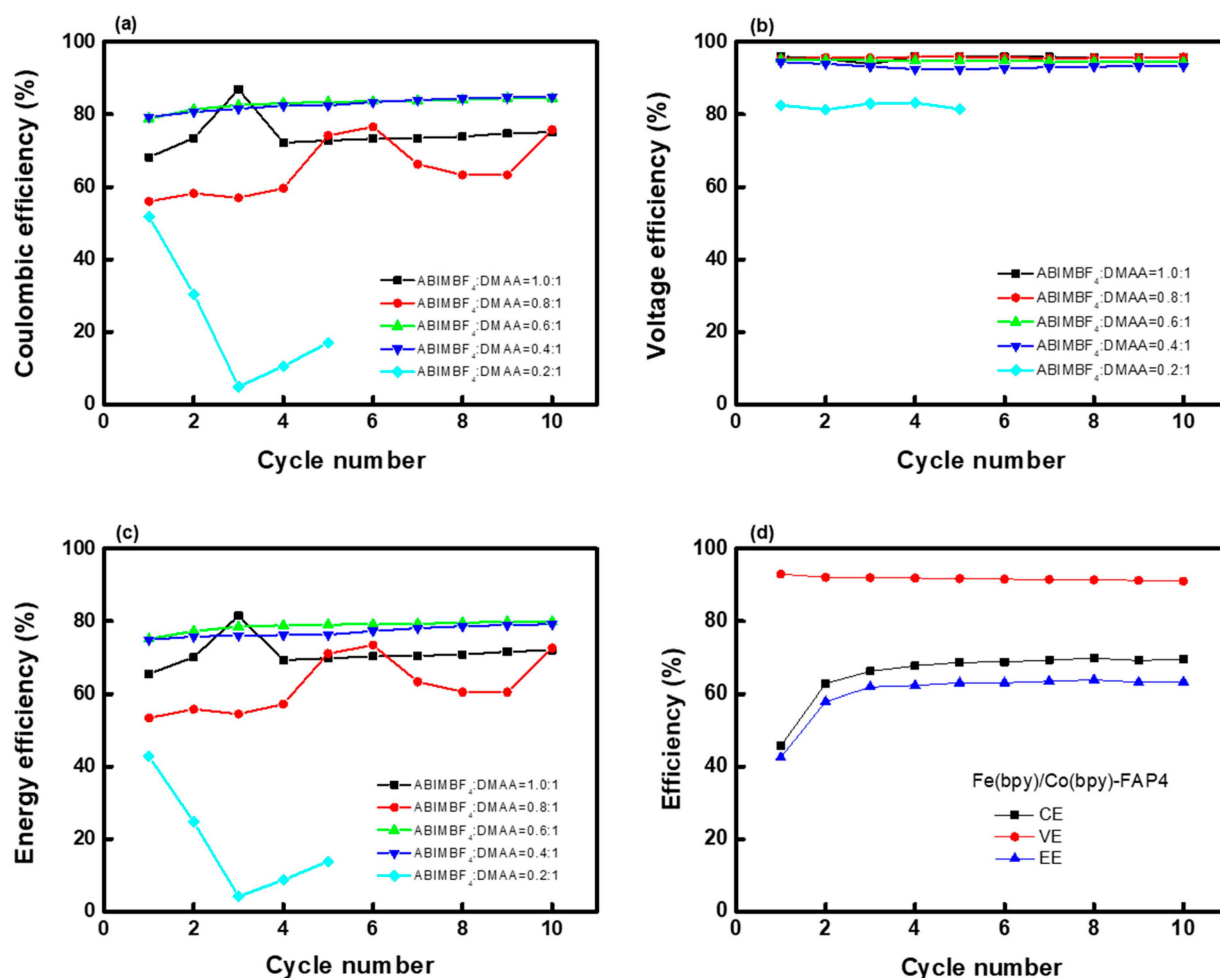| Membranes	$P\_Fe(bpy)_3^{2+}$ (cm^2/s)
FAP4 (Fumatech)	9.72×10^{-9}
PFAEM ($ABIMBF_4$:DMAA = 0.6:1)	1.56×10^{-12}

Figure 9. NARFB performances: (**a**) CE, (**b**) VE, (**c**) EE (PFAEMs prepared with different molar ratios of ABIMBF₄:DMAA), and (**d**) efficiencies (FAP4).

The durability of the membrane is crucial for the long-term operation and cost-effective maintenance of the NARFB process. Therefore, in this study, the durability of the membrane was assessed by comparing the characteristics of fresh membranes and those used in NARFB after the 100th charge–discharge cycle. Figure 10 displays the *I–V* and chronopotentiometry curves of PFAEM before and after the NARFB experiment. The results indicated only minor differences in both the *I–V* and chronopotentiometry curves before and after the charge–discharge test, signifying that the electrochemical properties of an IEM were well maintained. In addition, the changes in various membrane properties before and after the NARFB experiment are summarized in Table 6. After 100 cycles of charge–discharge experiments, the resistance of the membrane increased, and the TN decreased. This can be interpreted as a result of the reduction in the ion exchange groups and the increase in the free volume, as proven using the IEC and WU data. The decrease in the TN is also confirmed using the increase in the LCD value determined from the *I–V* curves. Furthermore, the ε value obtained from the chronopotentiometric curves indicates a slight reduction in the proportion of ion exchange groups on the membrane surface. However, it was observed that the changes in all the membrane performance parameters were insignificant, thereby confirming that the fabricated PFAEM possesses considerable durability for use in non-aqueous environments.
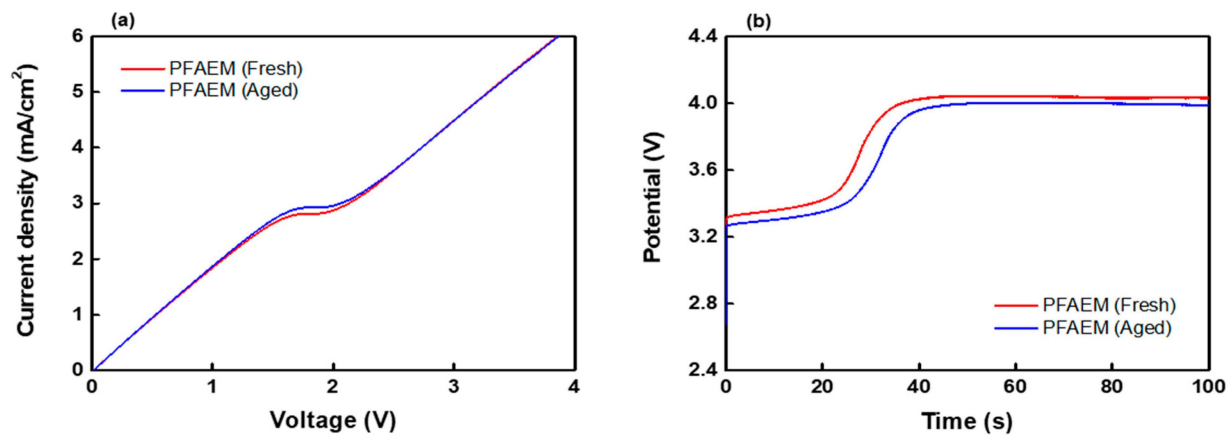
Figure 10. (**a**) *I–V* curves and (**b**) chronopotentiometric curves of PFAEM before (fresh) and after (aged) NARFB test.

Table 6. Characteristics of PFAEM before (fresh) and after (aged) NARFB test.

Membranes	WU (%)	IEC (meq./g)	MER [1] (Ω cm^2)	σ [2] (mS/cm)	TN (-)	LCD (mA/cm^2)	ε (-)
PFAEM (fresh)	32.35	2.01	2.18	1.15	0.972	2.80	0.904
PFAEM (aged)	40.48	1.89	2.68	0.93	0.938	2.93	0.895

[1] MER measured in 0.5 M NaCl aqueous solution. [2] Ion conductivity measured in 0.5 M NaCl solution (membrane thickness = 25 μm).

Figure 11 shows the change in efficiencies of the NARFB employing PFAEM for 100 cycles. The results demonstrated that the PFAEM fabricated in this study displayed relatively stable performance throughout the 100 cycles. The gradual decrease in VE is mainly due to the reduction in ion exchange groups and the consequent increase in electrical resistance, as shown in Table 6. Additionally, contamination of the membrane surface by metal complex redox species may have partially influenced the decrease in VE. In contrast, the CE remained stable, exhibiting a high EE of about 85% based on the 100th cycle.
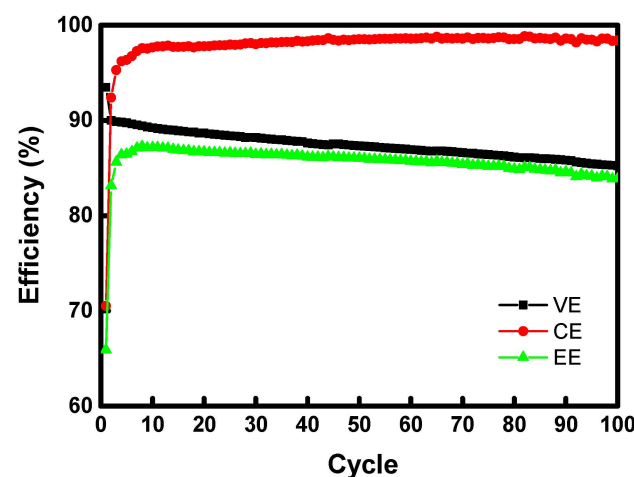

Figure 11. Changes in efficiencies of NARFB employing PFAEM for 100 cycles.

4. Conclusions

In this study, we developed novel PFAEMs tailored for use in NARFB systems that employ Fe/Co-metal complex redox species. These PFAEMs were prepared by infusing an anion-exchange polymer into the pores of a porous PE support, which has a thickness of about 25 μm. The process involved the copolymerization of ABIMBF$_4$, containing

allyl and imidazolium groups, with DMAA through photopolymerization. Additionally, dimethacrylate-based crosslinking agents were used to enhance the physical and chemical stability of the membranes. Out of the four reagents tested, EGDMA was selected as the crosslinker due to its lowest membrane resistance and highest selectivity. The fabricated PFAEMs exhibited excellent physical strength, a characteristic attributed to the intrinsic properties of the support material used in the membrane fabrication. Moreover, the PFAEMs showed very low resistance to BF_4^- ions in both aqueous and non-aqueous electrolyte solutions, a result of the molecular imprinting effect. We also focused on establishing optimal membrane fabrication conditions suitable for NARFB by adjusting the molar ratio of $ABIMBF_4$ to DMAA. The results indicated that membranes prepared in the $ABIMBF_4$:DMAA ratio range of 0.4–0.6:1 had moderate membrane resistance and low crossover properties of metal redox ion species, making them ideal for NARFB operation. Furthermore, the membrane fabricated under these optimal conditions demonstrated a 32% improvement in EE compared to the commercial Fumatech FAP4 membrane, based on the 10th cycle. Durability assessment revealed that the membrane maintained its intrinsic properties over 100 cycles of NARFB operation, although a slight decrease in IEC and a consequent increase in resistance were observed. Additionally, while there was a gradual decrease in VE over the 100-cycle operation, the overall charge–discharge performance remained stable, and a high EE of about 85% was confirmed based on the 100th cycle. The findings of this study are expected to contribute valuable insights for the development of high-performance IEMs, enhancing the performance of NARFBs currently under research and development.

Data Availability Statement: Data are contained within the article.

Conflicts of Interest: Myung-Jin Lee was employed by Samsung Advanced Institute of Technology. The remaining authors declare that the research was conducted in the absence of any commercial or financial relationships that could be construed as a potential conflict of interest.

References

1. Mitali, J.; Dhinakaran, S.; Mohamad, A.A. Energy storage systems: A review. *Energy Storage Sav.* **2022**, *1*, 166–216. [CrossRef]
2. Gür, T.M. Review of electrical energy storage technologies, materials and systems: Challenges and prospects for large-scale grid storage. *Energy Environ. Sci.* **2018**, *11*, 2696–2767. [CrossRef]
3. Sun, C.-N.; Mench, M.M.; Zawodzinski, T.A. High performance redox flow batteries: An analysis of the upper performance limits of flow batteries using non-aqueous solvents. *Electrochim. Acta* **2017**, *237*, 199–206. [CrossRef]
4. Hollas, A.; Wei, X.; Murugesan, V.; Nie, Z.; Li, B.; Reed, D.; Liu, J.; Sprenkle, V.; Wang, W. A biomimetic high-capacity phenazine-based anolyte for aqueous organic redox flow batteries. *Nat. Energy* **2018**, *3*, 508–514. [CrossRef]
5. Runa, M.; Alghamdi, N.; Peng, X.; Huang, Y.; Wang, B.; Wang, L.; Gentle, I.R.; Hickey, S.; Luo, B. Scientific issues of zinc-bromine flow batteries and mitigation strategies. *Exploration* **2023**, *3*, 20220073. [CrossRef]
6. Cabrera, P.J.; Yang, X.; Suttil, J.A.; Hawthorne, K.L.; Brooner, R.E.; Sanford, M.S.; Thompson, L.T. Complexes containing redox noninnocent ligands for symmetric, multielectron transfer nonaqueous redox flow batteries. *J. Phys. Chem. C* **2015**, *119*, 15882–15889. [CrossRef]
7. Sharma, S.; Andrade, G.A.; Maurya, S.; Popov, I.A.; Batista, E.R.; Davis, B.L.; Mukundan, R.; Smythe, N.C.; Tondreau, A.M.; Yang, P. Iron-iminopyridine complexes as charge carriers for non-aqueous redox flow battery applications. *Energy Storage Mater.* **2021**, *37*, 576–586. [CrossRef]
8. Yan, Y.; Vaid, T.P.; Sanford, M.S. Bis(diisopropylamino) cyclopropenium-arene cations as high oxidation potential and high stability catholytes for non-aqueous redox flow batteries. *J. Am. Chem. Soc.* **2020**, *142*, 17564–17571. [CrossRef]
9. Chai, J.; Lashgari, A.; Cao, Z.; Williams, C.K.; Wang, X.; Dong, J.; Jiang, J. PEGylation-enabled extended cyclability of a non-aqueous redox flow battery. *ACS Appl. Mater. Interfaces* **2020**, *12*, 15262–15270. [CrossRef]

10. Tung, S.; Fisher, S.L.; Kotov, N.A.; Thompson, L.T. Nanoporous aramid nanofibre separators for nonaqueous redox flow batteries. *Nat. Commun.* **2018**, *9*, 4193–4201. [CrossRef]
11. Li, Y.; Sniekers, J.; Malaquias, J.C.; Van Goethem, C.; Binnemans, K.; Fransaer, J.; Vankelecom, I.F. Crosslinked anion exchange membranes prepared from poly (phenylene oxide)(PPO) for non-aqueous redox flow batteries. *J. Power Sources* **2018**, *378*, 338–344. [CrossRef]
12. Huang, Y.; Gu, S.; Yan, Y.; Li, S.F.Y. Nonaqueous redox-flow batteries: Features, challenges, and prospects. *Curr. Opin. Chem. Eng.* **2015**, *8*, 105–113. [CrossRef]
13. Cammack, C.X.; Pratt, H.D.; Small, L.J.; Anderson, T.M. A higher voltage Fe (II) bipyridine complex for non-aqueous redox flow batteries. *Dalton Trans.* **2021**, *50*, 858–868. [CrossRef] [PubMed]
14. Davis, C.M.; Boronski, C.E.; Yang, T.; Liu, T.; Liang, Z. Molecular Engineering of Redox Couples for Non-Aqueous Redox Flow Batteries. *Batteries* **2023**, *9*, 504. [CrossRef]
15. Gong, K.; Fang, Q.; Gu, S.; Li, S.F.Y.; Yan, Y. Nonaqueous redox-flow batteries: Organic solvents, supporting electrolytes, and redox pairs. *Energy Environ. Sci.* **2015**, *8*, 3515–3530. [CrossRef]
16. Xu, T. Ion exchange membranes: State of their development and perspective. *J. Membr. Sci.* **2005**, *263*, 1–29. [CrossRef]
17. Kosswattaarachchi, A.M.; Cook, T.R. Concentration-dependent charge-discharge characteristics of non-aqueous redox flow battery electrolyte combinations. *Electrochim. Acta* **2018**, *261*, 296–306. [CrossRef]
18. Chai, J.; Lashgari, A.; Wang, X.; Williams, C.K.; Jiang, J. All-PEGylated redox-active metal-free organic molecules in non-aqueous redox flow battery. *J. Mater. Chem. A* **2020**, *8*, 15715–15724. [CrossRef]
19. Hendriks, K.H.; Sevov, C.S.; Cook, M.E.; Sanford, M.S. Multielectron Cycling of a low-potential anolyte in alkali metal electrolytes for nonaqueous redox flow batteries. *ACS Energy Lett.* **2017**, *2*, 2430–2435. [CrossRef]
20. Kwon, H.-G.; Bae, I.; Choi, S.-H. Crosslinked poly (arylene ether ketone) membrane with high anion conductivity and selectivity for non-aqueous redox flow batteries. *J. Membr. Sci.* **2021**, *620*, 118928. [CrossRef]
21. Mazumder, M.M.R.; Jadhav, R.G.; Minteer, S.D. Phenyl Acrylate-Based Cross-Linked Anion Exchange Membranes for Non-aqueous Redox Flow Batteries. *ACS Mater. Au* **2023**, *3*, 557–568. [CrossRef] [PubMed]
22. Mun, J.; Lee, M.-J.; Park, J.-W.; Oh, D.-J.; Lee, D.-Y.; Doo, S.-G. Non-aqueous redox flow batteries with nickel and iron tris (2,2′-bipyridine) complex electrolyte. *Electrochem. Solid-State Lett.* **2012**, *15*, A80. [CrossRef]
23. Park, M.-S.; Lee, N.-J.; Lee, S.-W.; Kim, K.J.; Oh, D.-J.; Kim, Y.-J. High-energy redox-flow batteries with hybrid metal foam electrodes. *ACS Appl. Mater. Interfaces* **2014**, *6*, 10729–10735. [CrossRef] [PubMed]
24. Kim, D.-H.; Seo, S.-J.; Lee, M.-J.; Park, J.-S.; Moon, S.-H.; Kang, Y.S.; Choi, Y.-W.; Kang, M.-S. Pore-filled anion-exchange membranes for non-aqueous redox flow batteries with dual-metal-complex redox shuttles. *J. Membr. Sci.* **2014**, *454*, 44–50. [CrossRef]
25. Veerman, J.; Gómez-Coma, L.; Ortiz, A.; Ortiz, I. Resistance of ion exchange membranes in aqueous mixtures of monovalent and divalent ions and the effect on reverse electrodialysis. *Membranes* **2023**, *13*, 322. [CrossRef]
26. Hagesteijn, K.F.L.; Jiang, S.; Ladewig, B.P. A review of the synthesis and characterization of anion exchange membranes. *J. Mater. Sci.* **2018**, *53*, 11131–11150. [CrossRef]
27. Klaysom, C.; Moon, S.-H.; Ladewig, B.P.; Lu, G.M.; Wang, L. Preparation of porous ion-exchange membranes (IEMs) and their characterizations. *J. Membr. Sci.* **2011**, *371*, 37–44. [CrossRef]
28. Jeevananda, T.; Yeon, K.-H.; Moon, S.-H. Synthesis and characterization of bipolar membrane using pyridine functionalized anion exchange layer. *J. Membr. Sci.* **2006**, *283*, 201–208. [CrossRef]
29. Jia, C.; Liu, J.; Yan, C. A significantly improved membrane for vanadium redox flow battery. *J. Power Sources* **2010**, *195*, 4380–4383. [CrossRef]
30. Bang, H.S.; Kim, D.; Hwang, S.S.; Won, J. Surface-modified porous membranes with electrospun Nafion/PVA fibres for non-aqueous redox flow battery. *J. Membr. Sci.* **2016**, *514*, 186–194. [CrossRef]
31. Lu, W.; Shao, Z.-G.; Zhang, G.; Li, J.; Zhao, Y.; Yi, B. Preparation of anion exchange membranes by an efficient chloromethylation method and homogeneous quaternization/crosslinking strategy. *Solid State Ion.* **2013**, *245*, 8–18. [CrossRef]
32. Jheng, L.-C.; Hsu, C.-Y.; Yeh, H.-Y. Anion exchange membranes based on imidazoline quaternized polystyrene copolymers for fuel cell applications. *Membranes* **2021**, *11*, 901. [CrossRef]
33. Balan, V.; Mihai, C.; Cojocaru, F.; Uritu, C.; Dodi, G.; Botezat, D.; Gardikiotis, I. Vibrational spectroscopy fingerprinting in medicine: From molecular to clinical practice. *Materials* **2019**, *12*, 2884. [CrossRef]
34. Wang, W.; Li, S. Improvement of dielectric breakdown performance by surface modification in polyethylene/TiO₂ nanocomposites. *Materials* **2019**, *12*, 3346. [CrossRef]
35. Łyszczek, R.; Podkościelna, B.; Lipke, A.; Ostasz, A.; Puszka, A. Synthesis and thermal characterization of luminescent hybrid composites based on bisphenol A diacrylate and NVP. *J. Therm. Anal. Calorim.* **2019**, *138*, 4463–4473. [CrossRef]
36. Shin, W.S.; Li, X.F.; Scgwartz, B.; Wunder, S.L.; Baran, G.R. Determination of the degree of cure of dental resins using Raman and FT-Raman spectroscopy. *Dent. Mater.* **1993**, *9*, 317–324. [CrossRef]
37. Lei, M.; Zhang, Q.; Chi, M.; Yu, Y.; Jiang, H.; Wang, S.; Min, D. Anion Exchange membrane with High hydroxide ion conductivity and robust tensile strength fabricated from quaternary ammonia functionalized *Pinus contorta, Dougl.* Chip. *Ind. Crops Prod.* **2021**, *166*, 113458. [CrossRef]

38. Khan, M.I.; Mondal, A.N.; Tong, B.; Jiang, C.; Emmanuel, K.; Yang, Z.; Wu, L.; Xu, T. Development of BPPO-based anion exchange membranes for electrodialysis desalination applications. *Desalination* **2016**, *391*, 61–68. [CrossRef]

39. Kaneto, K.; Hata, F.; Uto, S. Structure and size of ions electrochemically doped in conducting polymer. *J. Micromech. Microeng.* **2018**, *28*, 054003. [CrossRef]

40. Kubota, S.; Ozaki, S.; Onishi, J.; Kano, K.; Shirai, O. Selectivity on ion transport across bilayer lipid membranes in the presence of gramicidin A. *Anal. Sci.* **2009**, *25*, 189–193. [CrossRef]

41. Sillars, F.B.; Fletcher, S.I.; Mirzaeian, M.; Hall, P.J. Variation of electrochemical capacitor performance with room temperature ionic liquid electrolyte viscosity and ion size. *Phys. Chem. Chem. Phys.* **2012**, *14*, 6094–6100. [CrossRef]

42. Yoshikawa, M.; Tharpa, K.; Dima, S. Molecularly imprinted membranes: Past, present, and future. *Chem. Rev.* **2016**, *116*, 11500–11528. [CrossRef]

43. ul Haq, O.; Choi, J.; Lee, Y. Anion-exchange membrane for membrane capacitive deionization prepared via pore-filling polymerization in a porous polyethylene supporting membrane. *React. Funct. Polym.* **2018**, *132*, 36–42. [CrossRef]

44. Lehmann, M.L.; Tyler, L.; Self, E.C.; Yang, G.; Nanda, J.; Saito, T. Membrane design for non-aqueous redox flow batteries: Current status and path forward. *Chem* **2022**, *8*, 1611–1616. [CrossRef]